

Amorphization of wollastonite and diopside by ball milling

Yoshitaka MUROUCHI,^{1,*} Masayuki OKUNO,¹ and Naoya SASAKI²

¹ Department of Earth Science, Graduate School of Science and Technology, Kanazawa University,
Kanazawa, 920-1192, Japan

² Kutani Ware Research Center, Industrial Research Institute of Ishikawa,
Komatsu, 923-0151, Japan

(Received December 22, 2020 and accepted in revised form February 3, 2021)

Abstract The amorphization of wollastonite (CaSiO_3) and diopside ($\text{CaMgSi}_2\text{O}_6$) crystals by conventional ball milling under the dry condition and the atomic-scale structures of their amorphous phases were investigated by powder X-ray diffraction (XRD) analysis and Fourier transformed infrared (FT-IR) spectroscopy. The obtained results indicate that both wollastonite and diopside crystals were almost amorphized by ball milling. Moreover, the wollastonite crystal amorphized faster than the diopside crystal. The atomic-scale structures of the amorphous phases in the milled wollastonite and diopside obtained by X-ray radial distribution analyses were approximately similar to those in the fused glasses of wollastonite and diopside, respectively. However, FT-IR data may indicate that the single chains of SiO_4 tetrahedra remained as the dominant species even in the wollastonite and diopside subjected to prolonged ball milling.

Keywords. Ball milling, Amorphization, Inosilicate, Wollastonite, Diopside

1 Introduction

Wollastonite (CaSiO_3) is one of the pyroxenoid-group minerals, and diopside ($\text{CaMgSi}_2\text{O}_6$) is a clinopyroxene mineral. They are major rock-forming minerals and inosilicates, with single chains of SiO_4 tetrahedra. The wollastonite has excellent biological activity forming hydroxyapatite ($\text{Ca}_{10}(\text{PO}_4)_6(\text{OH})_2$) and binding to bones. However, its degradation rate is too fast, and its mechanical properties are inferior. By contrast, the diopside has higher mechanical properties given its slow degradation rate. Garcia et al. [1] reported that sprayed amorphous wollastonite and wollastonite-diopside compositions are useful new bioactive coating materials for metal implants to bones. Recently, artificial bones could be easily made with a three-dimensional (3D) printer. Especially for a selective laser sintering printer, ceramics and metals with a high melting point are suitable for powder source materials. Hence, wollastonite, diopside, their mixed crystals, and their glass powders have received much attention as bioceramics and bioglasses [2–8].

On the other hand, numerous milling experiments have been conducted on various minerals such as quartz, kaolinite, talc, and feldspar [9–11]. Disordered surface and hydrated phases are formed on the diopside by ball milling and dissolution [12,13]. Kalinkina et al. [14,15] and Kalinkin et al. [16] reported

* Corresponding author Email: murouchiy@yahoo.co.jp

that both wollastonite and diopside absorbed atmospheric water vapor and carbon dioxide, and α -quartz crystallized during milling by agate (SiO_2) pestle-and-mortar under open atmospheric conditions. However, they did not describe the amorphization of the wollastonite and diopside by mechanical milling and the atomic-scale structures of their amorphous phases. Their atomic-scale structures may be helpful for bioceramic design. Therefore, our significant aims in this study are to precisely investigate the amorphization processes of the wollastonite and diopside milled under dry conditions and analyzed the atomic-scale structures of their amorphous phases. Obtained atomic-scale structures are compared with those in their fused glasses.

2 Experimental

Specimens and chemical analysis

Polycrystalline white wollastonite was obtained from the Kiku mine at Fukuoka, Japan, and monocrystalline light-green diopside with a particle size of 10–20 μm was obtained from block D at Merelani, Tanzania. The densities of the original specimens were measured at room temperature by a buoyancy method as a reference. The observed wollastonite and diopside densities were $\rho = 2.85$ and 3.25 g/cm^3 , respectively.

Their chemical compositions were evaluated by electron microprobe analysis (EPMA: JXA-8800; JEOL, Japan) with the ZAF correction procedure. The measurement conditions consisted of an acceleration voltage of 20 kV, a beam current of 50 nA, and a probe diameter of 3 μm . Standard materials adopted natural wollastonite for Ca and Si, natural jadeite for Na, synthetic samples of Al_2O_3 , MgO, KTiPO_4 , Fe_2O_3 , Cr_2O_3 , MnO, and NiO for Al, Mg, K and Ti, Fe, Cr, Mn, and Ni, respectively.

Preparation of milled samples of wollastonite and diopside crystals

We prepared milled samples of wollastonite and diopside crystals using the following procedure. The original specimens were roughly ground using a tungsten carbide cylinder mortar and then passed through a 30 mesh (595 μm) sieve. These samples are referred to hereafter as the “initial” samples. Approximately 9.5 g of each initial sample and 40 ceramic balls 20 mm in diameter (94.92 mass% of $\text{ZrO}_2 + \text{HfO}_2$ and 4.81 mass% of Y_2O_3) were placed in a 2000-mL alumina vessel (93.0 mass% of Al_2O_3 and 7.0 mass% of SiO_2). A desktop pot mill (PM-001; AS ONE, Japan) operated at a rotational speed of 100 rpm was used in all batches at room temperature. The vessel was sealed during milling. The milled samples were collected in 1.0 g batches after 2, 16, 67, and 317 h of milling and after 512 h of milling in the diopside case. These samples are identified as “wollastonite-*T*h” and “diopside-*T*h,” where *T* denotes the milling time. The milled samples remaining in the vessel were dried in an oven at 80 °C for 10 min after each sampling to avoid atmospheric water vapor absorption.

Preparation of fused glasses for wollastonite and diopside

Approximately 0.50 g of each wollastonite and diopside crystal was separately placed in Pt crucibles and was melted at 1650 °C and 1500 °C, respectively, for 3 h in an electric furnace. These temperatures were higher than the melting points of pure wollastonite (1540 °C) and diopside (1342 °C) by 110 and 158 °C, respectively. The melts were rapidly quenched in the water to obtain fused glasses. The fused glass of wollastonite (wollastonite glass) was colorless and transparent; the fused glass of diopside (diopside glass) was light-green.

Particle size and its distribution measurements

All particle size distributions were measured using a laser scattering particle distribution analyzer (LA-920; HORIBA, Japan) in the $0.02 \leq d \leq 2000$ μm range. The particle size distribution of each specimen was measured at least twice, and their averaged data were used for this study. The characteristic diameters D_{10} , D_{50} , and D_{90} were calculated, averaging the median values. The diameters D_{10} , D_{50} , and D_{90} correspond to the apertures related to 10, 50, and 90 % passing of material, respectively. Preparations were carried out with ethanol ($\text{C}_2\text{H}_5\text{OH}$) and distilled water as dispersion solvent of wet method using a homogenizer. Their dispersion time of the homogenizer were for 2 minutes. The relative refractive indexes for wollastonite and diopside were 1.24 and 1.28, respectively.

Scanning electron microscopy (SEM)

The particle size and shape of wollastonite-2h, wollastonite-317h, diopside-2h, and diopside-512h were observed by SEM (JSM-7100F; JOEL, Japan) at the Industrial Research Institute of Ishikawa, Japan. The milled samples were attached to carbon tape and subsequently coated with an Au layer. SEM images were acquired with 15 kV secondary electrons.

Powder X-ray diffraction (XRD) measurements

Powder XRD patterns were measured with an X-ray powder diffractometer (RINT 2200; Rigaku, Japan) operated at an acceleration voltage and current of 40 kV and 30 mA, respectively. The initial and milled samples were placed on a glass sample holder and scanned using $\text{Cu K}\alpha$ monochromatic radiation; the data sampling interval was $2\theta = 0.02^\circ$, the scanning speed was $2\theta = 2.0^\circ/\text{min}$, and the scanning range was $2 \leq 2\theta \leq 120^\circ$.

Calculation of correlation function $G(r)$

To obtain the atomic-scale structure parameter, such as atomic pair distances, the author carried out another powder XRD measurements for wollastonite-317h, diopside-512h, wollastonite glass, and diopside glass under the following conditions. Each sample was placed on a brass sample holder and XRD measurements carried out with $\text{Mo K}\alpha$ monochromatic radiation using a step-scanning method in increments of $2\theta = 0.5^\circ$ in the range $2 \leq 2\theta \leq 140^\circ$ for fixed-time measurements of 1000 s. In addition, the XRD pattern of $\alpha\text{-Al}_2\text{O}_3$ reagent was measured under the same conditions because of the correction for small contamination of $\alpha\text{-Al}_2\text{O}_3$ from the vessel. All of the obtained data were corrected for absorption factor and normalized by the Krogh-Moe and Norman method [17]. Based on these corrected data, the procedure described by Marumo and Okuno [18] led to the interference function $S \cdot i(S)$, radial distribution function (RDF), and correlation function $G(r)$ of wollastonite-317h, diopside-512h, the wollastonite glass, and the diopside glass. For these calculations, the densities of wollastonite-317h and diopside-512h were measured by a gas-displacement pycnometry system (AccuPyc II 1340; Micromeritics, USA) were used. The measured densities of wollastonite-317h and diopside-512h were $\rho = 2.86$ and 2.76 g/cm^3 , respectively. The fused glasses' density data were used those reported by Shimoda et al. (2005): $\rho = 2.91$ g/cm^3 for CaSiO_3 glass and $\rho = 2.84$ g/cm^3 for $\text{CaMgSi}_2\text{O}_6$ glass.

Fourier transform infrared (FT-IR) spectroscopy

We recorded infrared (IR) spectra of all of the samples in ATR mode using FT-IR spectrometer (NICOLET iS10; Thermo Fisher Scientific, USA) equipped with a diamond crystal. The spectrum's wavenumber range was $\nu = 525\text{--}4000\text{ cm}^{-1}$, and its bandpass was $\nu = 4\text{ cm}^{-1}$.

3 Results

Chemical compositions

The chemical compositions obtained by EPMA analyses for the original specimens showed almost ideal chemical compositions of the wollastonite and diopside (Table 1). Namely, their impurity levels were low. For example, the MnO and NiO contents in the wollastonite specimen were less than 0.30 mass%. The Al₂O₃ content in the diopside specimen was less than 1.0 mass%, and the MnO and Na₂O contents in it were less than 0.2 mass%.

Table 1. Chemical compositions of the original specimens.

Mineral	(Units: wt.%)		Cation	(Units: Atomic ratio)	
	Wollastonite	Diopside		Wollastonite	Diopside
SiO ₂	51.19	54.83	Si ⁴⁺	1.981	1.972
TiO ₂	0.00	0.01	Ti ⁴⁺	0.000	0.000
Al ₂ O ₃	0.01	0.81	Al ³⁺	0.000	0.034
Cr ₂ O ₃	0.00	0.00	Cr ³⁺	0.000	0.000
FeO	0.00	0.09	Fe ³⁺	0.000	0.003
MnO	0.30	0.17	Fe ²⁺	0.000	0.000
NiO	0.16	0.01	Mn ²⁺	0.010	0.005
MgO	0.01	18.20	Ni ²⁺	0.005	0.000
CaO	48.29	25.89	Mg ²⁺	0.001	0.976
Na ₂ O	0.00	0.16	Ca ²⁺	2.002	0.998
K ₂ O	0.00	0.00	Na ⁺	0.000	0.011
Total	99.96	100.17	K ⁺	0.000	0.000
			Total	4	4

Particle size distributions and scanning electron microscopy (SEM) observations

Figures 1 and 2 show the particle size distributions of the milled wollastonite and diopside, respectively. Tables 2 and 3 show the diameters D_{10} , D_{50} , and D_{90} of the milled wollastonite and diopside, respectively. Both D_{50} decreased under $10\ \mu\text{m}$ for 2 h of milling. Then their peak shifted to around $30\ \mu\text{m}$ for 317 h of milling. The D_{50} of the wollastonite increased for 16 h of milling and then re-decreased to $D_{50} = 9.66\ \mu\text{m}$. By contrast, the D_{50} of the diopside increased for 317 h of milling and decreased to $D_{50} = 8.48\ \mu\text{m}$ for 512 h of milling.

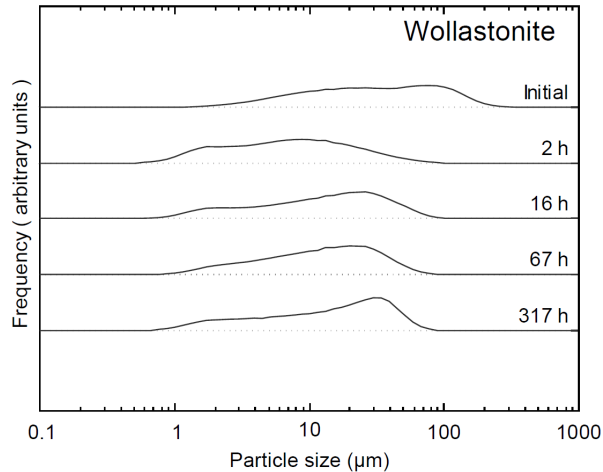


Figure 1. The particle size distribution of the wollastonite as a function of milling time.

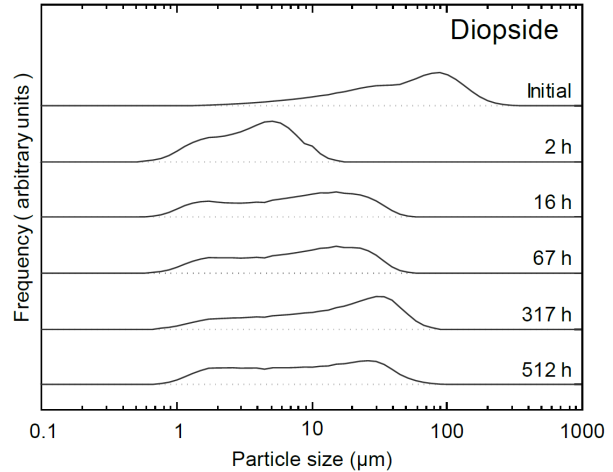


Figure 2. The particle size distribution of the diopside as a function of milling time.

Table 2. Diameters D_{10} , D_{50} , and D_{90} of the milled wollastonite as a function of milling time.

(Units: μm)			
Milling time	D_{10}	D_{50}	D_{90}
0 h	5.42	27.52	106.05
2 h	1.50	6.59	25.08
16 h	1.96	12.52	38.50
67 h	2.58	11.92	33.38
317 h	3.05	9.66	27.84

Table 3. Diameters D_{10} , D_{50} , and D_{90} of the milled diopside as a function of milling time.

(Units: μm)			
Milling time	D_{10}	D_{50}	D_{90}
0 h	8.81	47.05	119.75
2 h	1.26	3.52	7.53
16 h	1.39	7.57	24.35
67 h	1.56	8.09	24.47
317 h	2.14	14.67	38.90
512 h	1.63	8.48	31.84

Figure 3 shows the SEM images of wollastonite-2h, wollastonite-317h, diopside-2h, and diopside-512h. Many particles about $1\ \mu\text{m}$ were observed to adhere to a particle over $10\ \mu\text{m}$ size in the images of 2 h of milling. By contrast, the aggregation of small grains was observed in the images of wollastonite-317h and diopside-512h. The small particle size in the images of 2 h of milling was not much different from that of isolated small particles, and the particles included in aggregates particles in the images of wollastonite-317h and diopside-512h. Almost all particles were angular in the images of 2 h of milling.

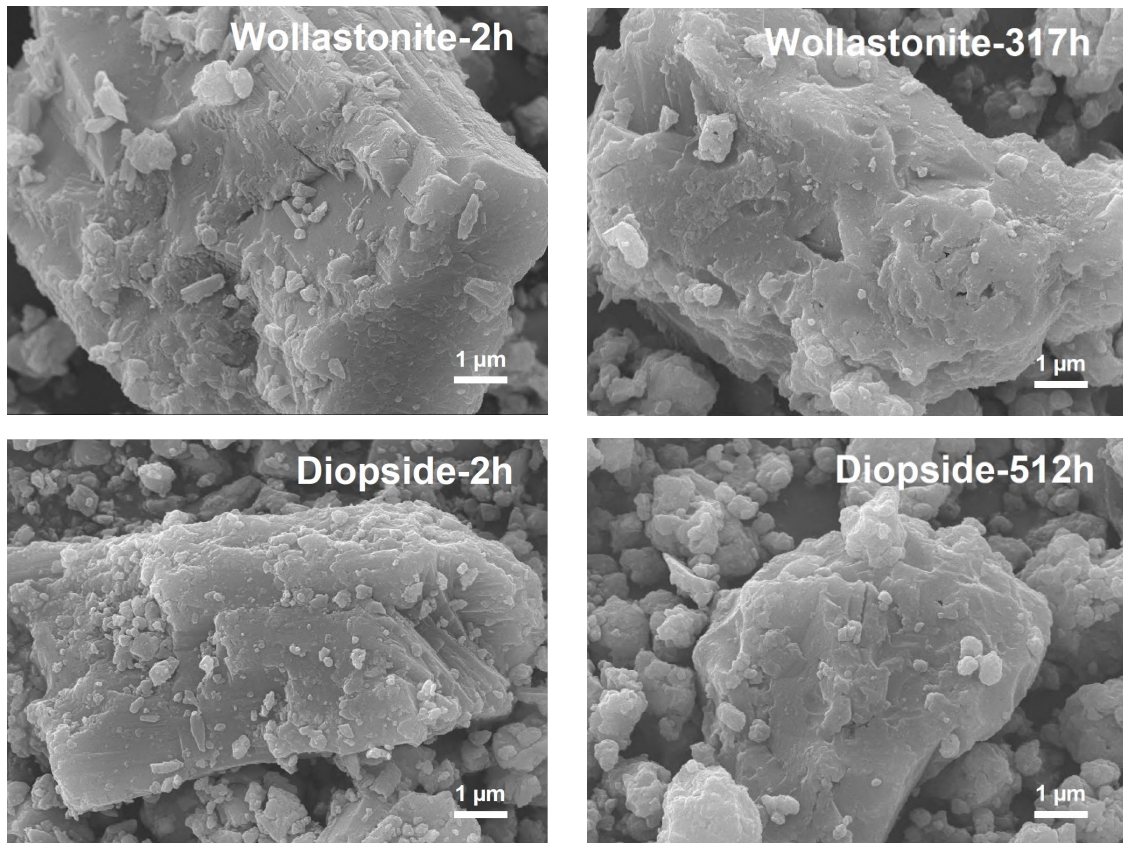


Figure 3. The SEM images of wollastonite-2h, wollastonite-317h, diopside-2h, and diopside-512h.

Many uniform spherical particles were observed in the images of wollastonite-317h and diopside-512h. Since inorganic nanoparticles such as SiO_2 are very easy to agglomerate, the aggregation was induced despite a dispersion process in particle size distribution measurements.

Powder X-ray diffraction (XRD) measurements

Figure 4 shows the XRD patterns of the initial and milled samples of the wollastonite. Although the sharp peak intensity at $2\theta = 30.00^\circ$ ($\bar{3}20$) increased, other peaks decreased for 2 h of milling. The intensities of all of the sharp peaks decreased after 2 h of milling. Finally, only a broad peak at $2\theta \approx 30^\circ$ was observed in the patterns of wollastonite-317h. Figure 5 shows the patterns of the initial and milled samples of the diopside. The intensities of almost all of the sharp peaks decreased for 2 h of milling. In particular, the intensities of the sharp peaks at 2θ angles of about 27° ($\bar{2}20$), 43° ($\bar{3}30$), 52° ($\bar{1}50$), and 72° ($\bar{5}33$) largely decreased. By contrast, the intensities of the sharp peaks at $2\theta = 29.84^\circ$ ($\bar{2}21$) and $2\theta = 35.62^\circ$ (221) increased for 2 h of milling. The intensities of all of the sharp peaks decreased after 2 h of milling. Finally, only a broad peak at $2\theta \approx 30^\circ$ was observed in the patterns of diopside-512h like wollastonite-317h. However, some new weak sharp peaks in the patterns of wollastonite-317h and diopside-512h were observed. These peaks entirely matched the peak positions of $\alpha\text{-Al}_2\text{O}_3$.

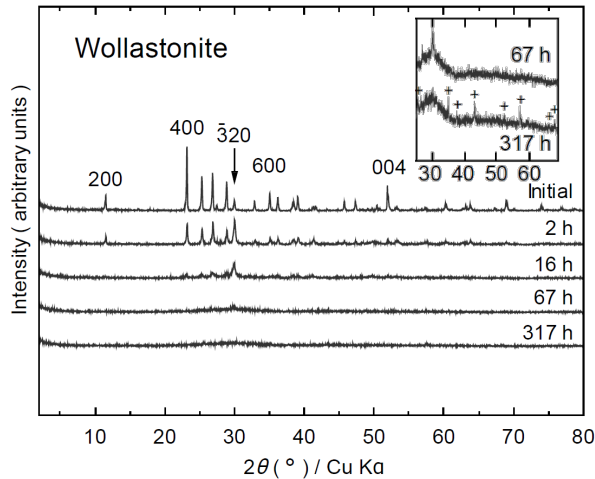


Figure 4. The XRD patterns of the wollastonite as a function of milling time. Plus (+) marks indicated the peak positions of α - Al_2O_3 .

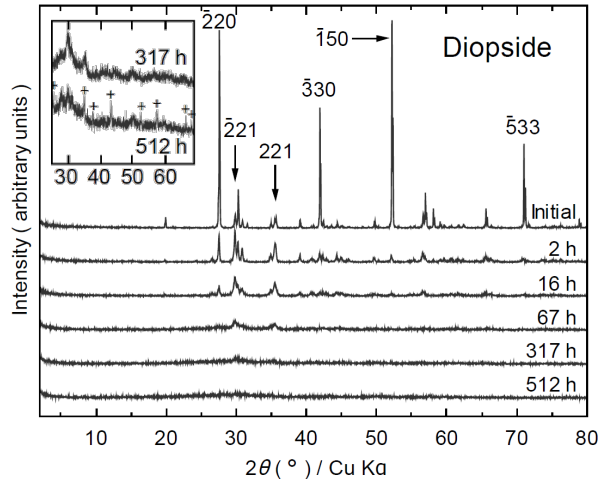


Figure 5. The XRD patterns of the diopside as a function of milling time. Plus (+) marks indicated the peak positions of α - Al_2O_3 .

Interference function $S \cdot i(S)$ and correlation function $G(r)$ curves

Figure 6 shows the XRD pattern with Mo $K\alpha$ monochromatic radiation of the wollastonite glass and the pattern which subtracted the effect of α - Al_2O_3 estimated from measured intensity under the same conditions for wollastonite-317h (317h - Al_2O_3), and Figure 7 shows those of the diopside glass and the pattern which subtracted the effect of α - Al_2O_3 estimated from measured intensity under the same conditions for diopside-512h (512h - Al_2O_3). Their patterns showed intense broad peaks at $2\theta \approx 13.5^\circ$. Two weak sharp peaks at $2\theta = 22.5^\circ$ and 26.5° remained in the pattern of diopside-512h corrected for α - Al_2O_3 .

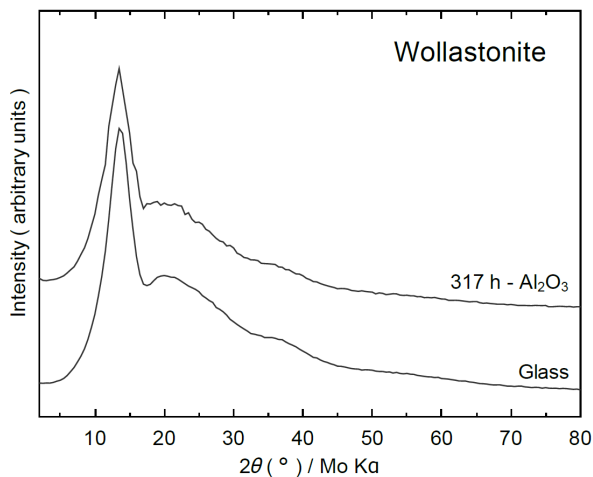


Figure 6. The XRD patterns of the wollastonite glass and wollastonite-317h corrected for α - Al_2O_3 .

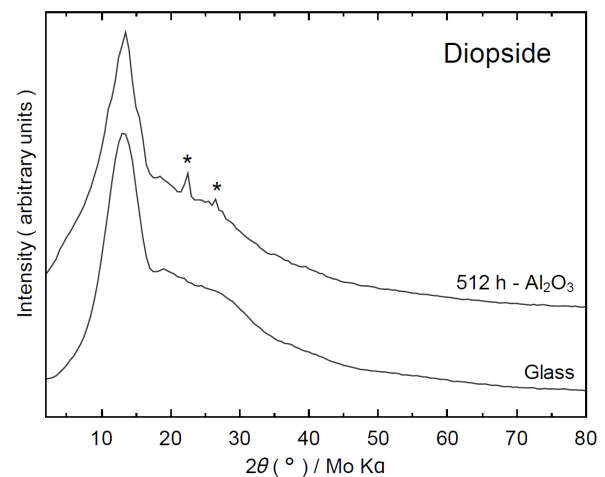


Figure 7. The XRD patterns of the diopside glass and diopside-512h corrected for α - Al_2O_3 . The weak sharp peaks showed by asterisk (*) marks were not that of α - Al_2O_3 .

The $S \cdot i(S)$ curves calculated from the XRD patterns for wollastonite-317h corrected for $\alpha\text{-Al}_2\text{O}_3$ contamination, the wollastonite glass, diopside-512h corrected for $\alpha\text{-Al}_2\text{O}_3$ contamination, and the diopside glass are shown in Figures 8 and 9.

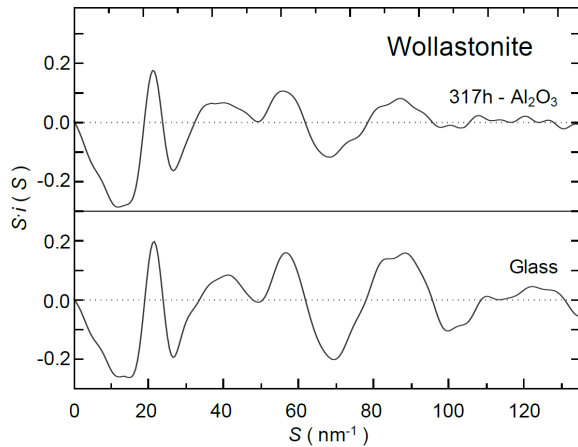


Figure 8. The $S \cdot i(S)$ curves of wollastonite-317h corrected for $\alpha\text{-Al}_2\text{O}_3$ and the wollastonite glass.

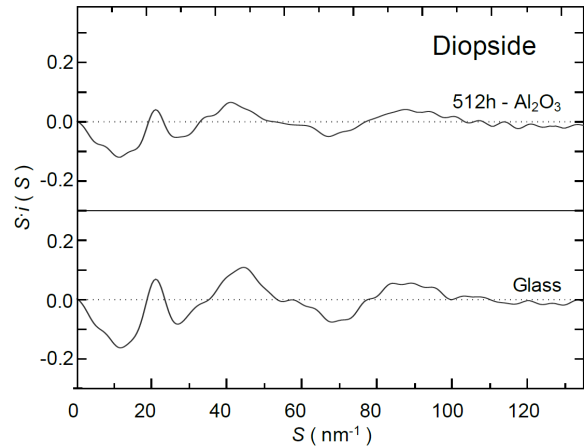


Figure 9. The $S \cdot i(S)$ curves of diopside-512h corrected for $\alpha\text{-Al}_2\text{O}_3$ and the diopside glass.

The $G(r)$ curves calculated from these $S \cdot i(S)$ data are shown in Figures 10 and 11. Maxima of $G(r)$ curves show the atomic pair distribution, such as Si–O atomic pairs in the samples. According to the previous studies on CaSiO_3 , MgSiO_3 , and $\text{CaMgSi}_2\text{O}_6$ glasses [19–21] and ionic radii data [22], the maximum at $0.160 \leq r \leq 0.164$ nm in the $G(r)$ curve was attributable to average Si–O atomic pairs in SiO_4 tetrahedra, that at $r \approx 0.24$ nm was an average of overlapped peaks of Ca–O, Mg–O, and O–O atomic pairs, and the shoulder or maximum at $r \approx 0.32$ nm was attributable to average Si–Si pairs between neighboring SiO_4 tetrahedra.

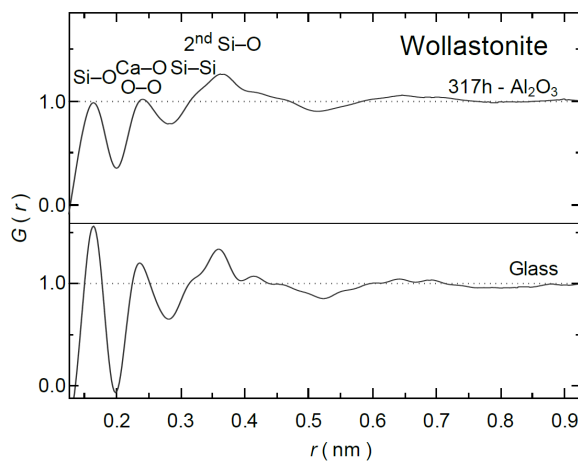


Figure 10. The $G(r)$ curves of wollastonite-317h corrected for $\alpha\text{-Al}_2\text{O}_3$ and the wollastonite glass.

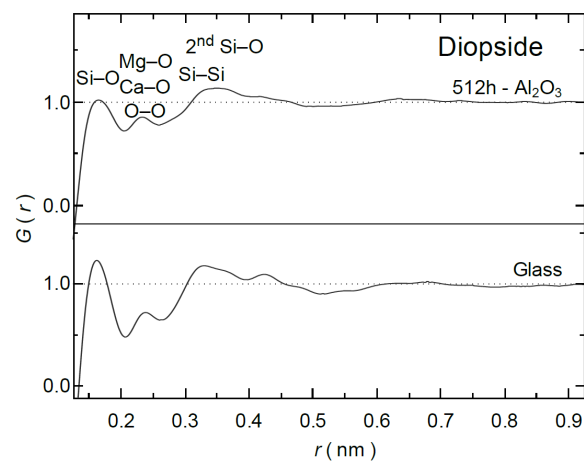


Figure 11. The $G(r)$ curves of diopside-512h corrected for $\alpha\text{-Al}_2\text{O}_3$ and the diopside glass.

Infrared (IR) spectroscopic analysis

The IR spectra of the initial and milled wollastonite samples are shown in Figure 12. The diopside ones are shown in Figure 13. Sharp absorption bands were observed in the $\nu = 550\text{--}600$, $600\text{--}700$, and $800\text{--}1250\text{ cm}^{-1}$ regions in both initial samples' spectra. Their sharp bands become broader with increasing milling time. After the prolonged ball milling, only the strong broad band remained at around $\nu = 918\text{ cm}^{-1}$ in the spectrum of wollastonite-317h and $\nu = 926\text{ cm}^{-1}$ in that of diopside-512h. Furthermore, new broad bands exhibited at $\nu = 665\text{ cm}^{-1}$ in the spectra of wollastonite-317h and diopside-512h. The very weak broad band at $\nu = 1400\text{--}1550\text{ cm}^{-1}$ was observed in all milled samples' spectra. Weak sharp bands and weak broad bands were observed in the $\nu = 550\text{--}600$ and $600\text{--}800\text{ cm}^{-1}$ regions, respectively, in the spectra of both wollastonite and diopside glasses. The strong broad band at around $\nu = 906\text{ cm}^{-1}$ was observed in the wollastonite glass' spectra, and that at around $\nu = 903\text{ cm}^{-1}$ was observed in the diopside glass' spectra.

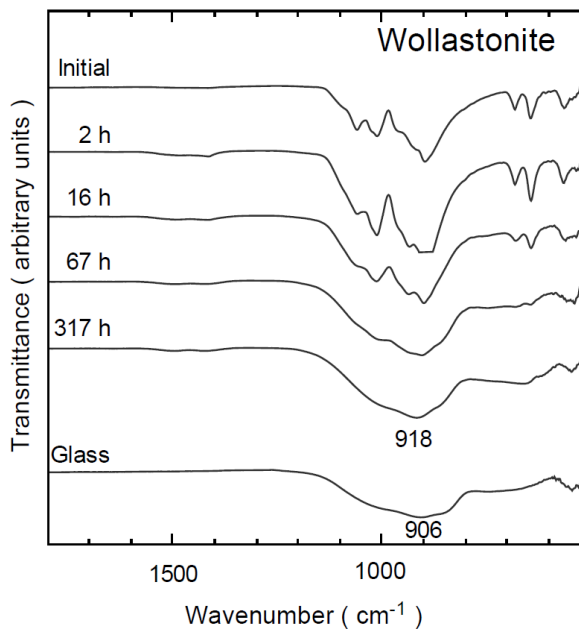


Figure 12. The IR spectra of the wollastonite as a function of milling time and its glass.

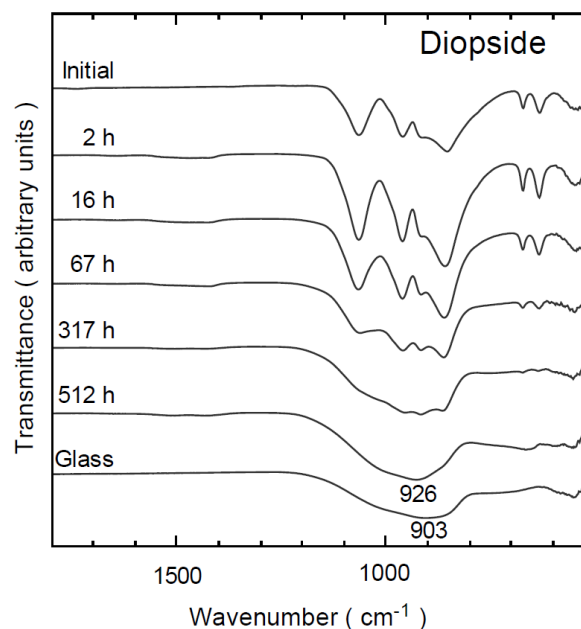


Figure 13. The IR spectra of the diopside as a function of milling time and its glass.

4 Discussion

Atmospheric effect on mechanical milling

Kalinkin et al. [16] reported that wollastonite and diopside were nearly amorphized by pestle-and-mortar milling. They also described α -quartz crystallization, resulting from atmospheric water vapor's catalytic effect during milling. However, the H_2O absorption bands at $\nu = 1650\text{ cm}^{-1}$ and $3300\text{--}3700\text{ cm}^{-1}$ are almost not detected in this study (Figs. 12 and 13) because we used the sealed vessel for ball milling to avoid the atmospheric water vapor's catalytic effect and dried its vessel after each sampling. This result is consistent with the absence of α -quartz in the XRD patterns and IR spectra. In previous studies [23,24], the CO_3^{2-} bands appeared in the $\nu = 1400\text{--}1550\text{ cm}^{-1}$ region in the IR spectrum. Moreover, Kalinkina et al. [14] reported that diopside milled for an extended duration contained more than 10 wt.% of CaCO_3

from its IR spectrum. However, in this study, the CO_3^{2-} band is very weak in all milled samples. Besides, we cannot find the peaks attributable to MgCO_3 , CaCO_3 , or $\text{CaMg}(\text{CO}_3)_2$ in the XRD patterns. Consequently, the milled samples absorb almost no atmospheric water vapor and little atmospheric carbon dioxide in this study.

Structure changes and amorphization by ball milling

As mentioned above, α -quartz and carbonates may not crystallize in the milled wollastonite and diopside. So, we discussed the amorphization of the wollastonite and diopside crystals during milling.

The IR sharp absorption bands of the initial wollastonite and diopside samples became broader with increasing milling time. However, the strong absorption band position at around $\nu = 920 \text{ cm}^{-1}$ (Si–O stretching vibrations of SiO_4 tetrahedra) does not almost change. These facts infer that the chain structure of SiO_4 tetrahedra keeps in the narrow range of the strong absorption band despite the prolonged ball milling. Furthermore, the IR spectra of wollastonite-317h and diopside-512h are similar to those of the wollastonite and diopside glasses, respectively (Figs. 12 and 13). However, there are some differences in the strong band position around $\nu = 920 \text{ cm}^{-1}$, and a new weak broad absorption band appeared at around $\nu = 665 \text{ cm}^{-1}$ in the spectra of wollastonite-317h and diopside-512h. Its band entirely matches the band positions of α - Al_2O_3 .

On the other hand, we observed substantial changes between the XRD patterns of the initial samples and the samples milled for 2 h (Figs. 4 and 5); the changes in the patterns of the diopside were particularly pronounced. This result indicates that the powder prepared from monocrystalline diopside keeps higher crystallinity than the powder prepared from polycrystalline wollastonite and is in agreement with the diopside D_{90} larger than wollastonite one. Besides, the intensities of the relative peaks in the patterns of the initial samples substantially differ from those in standard XRD patterns of wollastonite-2M (Powder Diffraction File (PDF) 43-1460 of International Centre for Diffraction Data (ICDD)) and diopside (PDF 41-1370). By contrast, the relative peaks' intensities in the patterns of the samples milled for 2 h are similar to those listed in the ICDD PDFs. Besides, the particle size distribution after 2h of milling (Fig. 1) is suitable for powder XRD measurements. Therefore, the peak intensities in the patterns of the samples milled for 2 h expressed more accurate intensities.

Figure 14 shows the integrated intensity ratio changes in the $2 \leq 2\theta \leq 120^\circ$ range of the XRD patterns for the milled wollastonite and diopside. After 2 h of milling, the integrated intensities in the patterns of the milled wollastonite decreased faster than those of the milled diopside. Mg–O ionic bond energy is greater than Ca–O one. Besides, the ionization energy of Mg^{2+} cations is larger than that of Ca^{2+} cations. Ca–O bonds are more friable than Mg–O bonds in inosilicates [25]. So, Mg^{2+} cations in the diopside strongly connect the single chains of SiO_4 tetrahedra. This result is consistent with diopside exhibiting greater hardness (Mohs hardness $5\frac{1}{2}$ – $6\frac{1}{2}$) than wollastonite (Mohs hardness $4\frac{1}{2}$ –5). The XRD patterns of wollastonite-317h and diopside-512h were similar to those of the wollastonite and diopside glasses, respectively (Figs. 4–7). However, weak sharp peaks on the patterns of wollastonite-317h and diopside-512h are observed. We also found the additional band located at the $\nu = 665 \text{ cm}^{-1}$ in the IR spectra of wollastonite-317h and diopside-512h. These bands correspond to α - Al_2O_3 contamination (Figs. 12 and 13). This α - Al_2O_3 contamination may be due to the alumina vessel. Consequently, the XRD integrated intensities of wollastonite-317h and diopside-512h increased by small contamination of α - Al_2O_3 .

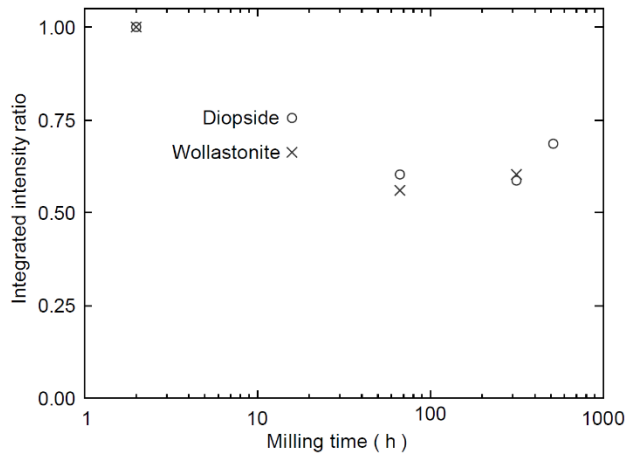


Figure 14. The XRD integrated intensity ratios in the $2 \leq 2\theta \leq 120^\circ$ range. The ratio for 2 h of milling was set to 1.00.

In summary, wollastonite and diopside crystal almost amorphized by prolonged ball milling without the α -quartz crystallization, even small contamination of α - Al_2O_3 . Moreover, small differences between the amorphous milled and glass samples were observed on $S \cdot i(S)$ and IR spectra. The next section will discuss their atomic-scale structures and the difference between those of the amorphous phases in the milled and glass samples.

Atomic-scale structures of amorphous phases

The $S \cdot i(S)$ curves include structural information for the amorphous phase. In this study, the $S \cdot i(S)$ curve of wollastonite-317h is roughly similar to that of the wollastonite glass. This result indicates that wollastonite-317h probably includes a small quantity of crystallite-like phase. The $S \cdot i(S)$ curve of diopside-512h is also similar to that of the diopside glass. However, the amplitudes of their milled samples are smaller than those of the glass samples. This result may indicate many variations of structure units such as linkages of SiO_4 tetrahedra in milled samples.

The $G(r)$ curves for the wollastonite and diopside glasses (Figs. 10 and 11) roughly match those reported in previous studies [20,21,26]. The calculated Si coordination number in wollastonite-317h and diopside-512h was 4.0–4.1. Hence, we consider that the basic structure units of their milled samples are the SiO_4 tetrahedra and consistent with the first maximum position ($0.160 \leq r_{\text{Si-O}} \leq 0.164$ nm) of their $G(r)$ curves. The attenuation distance (r_s) of the $G(r)$ curve in wollastonite-317h is similar to that in the wollastonite glass ($r_s > 8.0$ nm) (Fig. 10). The curve's attenuation distance in diopside-512h is similar to that in the diopside glass ($r_s \approx 7.0$ nm) (Fig. 11). $r_s/r_{\text{Si-O}}$ is known as short-range order parameters [20]. Those for wollastonite-317h and diopside-512h are 4.9 and 4.4, respectively. Yin et al. [20] reported that the short-range order parameter in CaSiO_3 glass (approximately 5.0) was larger than that in MgSiO_3 glass (approximately 4.4). The short-range order parameter is inverse proportion to Coulomb's force. Coulomb's force for Mg-O bonds with smaller Mg^{2+} cation is greater than that for Ca-O bonds with larger Ca^{2+} cation. Their results are consistent that the short-range order parameters in diopside-512h and the diopside glass are smaller than those in wollastonite-317h and the wollastonite glass, respectively. The amorphous phases in the milled wollastonite and diopside retain roughly similar short-range structures to those of the wollastonite and diopside glasses. However, not a little difference in the atomic-scale structures was found on the $S \cdot i(S)$ and $G(r)$ curves. Namely, the milled samples may have a similar structure to the crystalline phase.

Generally, the IR bands in the $\nu = 800\text{--}1250$ cm^{-1} region for silicates were assigned to Si-O asymmetric stretching vibrations within a SiO_4 tetrahedron [27,28]. Four bands at approximately $\nu = 870, 920, 990,$ and 1090 cm^{-1} in the spectrum of CaO-SiO_2 systems were assignable to Q^0 (monomer),

Q¹ (dimer), Q² (chain), and Q³ (sheet) species of SiO₄ tetrahedra, respectively [29]. CaSiO₃ and CaMgSi₂O₆ glasses had Q² as dominant species with contributions from Q⁰ and Q³ species [21,30]. In the present study, the absorption band at the $\nu = 918 \text{ cm}^{-1}$ of wollastonite-317h was located at a higher wavenumber position than the wollastonite glass one ($\nu = 906 \text{ cm}^{-1}$). Moreover, the band at the $\nu = 926 \text{ cm}^{-1}$ of diopside-512h was located at a higher wavenumber position than the diopside glass one ($\nu = 903 \text{ cm}^{-1}$). Furthermore, the shapes of the bands of wollastonite-317h and diopside-512h were sharper than those of the wollastonite and diopside glasses. These results are consistent with the discussion of the $S \cdot i(S)$ and $G(r)$ curves. Therefore, wollastonite-317h and diopside-512h may include a larger number of Q¹ and Q² species than the wollastonite and diopside glasses. It means that the single chains of SiO₄ tetrahedra may remain even in wollastonite-317h and diopside-512h despite the prolonged ball milling.

The IR bands in the $\nu = 600\text{--}700 \text{ cm}^{-1}$ region were assigned to Si–O–Si bending vibrations within a SiO₄ tetrahedron (Kubicki et al., 1992). In the present study, these sharp bottom bands in its region of the initial samples for the wollastonite and diopside become broader with increasing milling time and almost disappear in the spectra of wollastonite-317h and diopside-512h. Its result indicates that the Si–O–Si angles between neighboring SiO₄ tetrahedra in wollastonite-317h and diopside-512h have many variations, and some Si–O–Si bonds are broken.

5 Conclusions

In this study, based on the XRD measurements and IR spectroscopy, we investigated the amorphization processes of the wollastonite and diopside by ball milling and the atomic-scale structures of the amorphous phases obtained by prolonged ball milling. Our results showed almost no absorption of water vapor or carbon dioxide during the milling experiment. Furthermore, we found that the crystal phase of the wollastonite transformed into an amorphous phase easier than that of the diopside. This is because Mg–O bonds in the diopside connect stronger than Ca–O bonds. However, comparing the atomic-scale structures of the amorphized wollastonite and diopside with those of the wollastonite and diopside glasses, respectively, the single chains of SiO₄ tetrahedra remained well even in the milled wollastonite and diopside. We found that the amorphous wollastonite and diopside are easily obtained by ball milling, and they are expected as useful materials for 3D printers and bioactive implant use.

Acknowledgments

We express supreme thanks to Dr. M. Hamada of Kanazawa University for EPMA analyses. The authors are greatly indebted to the editors and two anonymous referees.

References

- [1] Garcia, E., Miranzo, P., and Sainz, M.A. (2018) Thermally sprayed wollastonite and wollastonite-diopside compositions as new modulated bioactive coatings for metal implants. *Ceramics International* 44, 12896-12904.
- [2] Magallanes-Pardomo, M., Luklinska, Z.B., De Aza, A.H., Carrodegua, R.G., and De Aza, S. et al. (2011) Bone-like forming ability of apatite–wollastonite glass ceramic. *Journal of the European Ceramic Society* 31, 1549–1561.
- [3] He, D., Zhuang, C., Xu, S., Ke, X., and Yang, X. et al. (2016) 3D printing of Mg-substituted wollastonite

- reinforcing diopside porous bioceramics with enhanced mechanical and biological performances. *Bioactive Materials* 1, 85–92.
- [4] Shao, H., He, Y., Fu, J., He, D., and yang, X. et al. (2016) 3D printing magnesium-doped wollastonite/ β -TCP bioceramics scaffolds with high strength and adjustable degradation. *Journal of the European Ceramic Society* 36, 1495–1503.
- [5] Hamada, E., Paolo, C., and Enrico, B. (2017) Direct ink writing of wollastonite–diopside glass-ceramic scaffolds from a silicone resin and engineered fillers. *Journal of the European Ceramic Society* 37, 4187–4195.
- [6] Zhang, L., Yang, G., Johnson, B.N., and Jia, X. (2019) Three-dimensional (3D) printed scaffold and material selection for bone repair. *Acta Biomaterialia* 84, 16–33.
- [7] Fu, S., Hu, H., Chen, J., Zhu, Y., and Zhao, S. (2020) Silicone resin derived larnite/C scaffolds via 3D printing for potential tumor therapy and bone regeneration. *Chemical engineering Journal* 382, 122928.
- [8] Kamboj, N., Kazantseva, J., Rahmani, R., and Rodriguez, M.A. (2020) Selective laser sintered bio-inspired silicon–wollastonite scaffolds for bone tissue engineering. *Materials Science & Engineering C* 116, 11223.
- [9] Sugiyama, K., Filio, J.M., Saito, F., and Waseda, Y. (1994) Structural change of kaolinite and pyrophyllite induced by dry grinding. *Mineralogical Journal* 17, 28–41.
- [10] Esteban, F.A. (1994) The effect of dry grinding on the structure of talc. *Applied Clay Science* 9, 139–147.
- [11] Nojiri, H., Okuno, M., Okudera, H., Mizukami, T. and Arai, S. (2013) Structural change of alkali feldspar by ball milling. *Journal of Mineralogical and Petrological Sciences* 108, 267–277.
- [12] Peck, J.A., Farnan, I., and Stebbins, J.F. (1988) Disordering and the progress of hydration at the surface of diopside: a cross-polarisation MAS-NMR study. *Geochimica et Cosmochimica Acta* 52, 3017–3021.
- [13] Eggleston, C.M., Hochella, M.F., JR., and Parks, G.A. (1989) Sample preparation and aging effects on the dissolution rate and surface composition of diopside. *Geochimica et Cosmochimica Acta* 53, 797–804.
- [14] Kalinkina, E.V., Kalinkin, A.M., Forsling, W., and Makarov, V.N. (2001) Sorption of atmospheric carbon dioxide and structural changes of Ca and Mg silicate minerals during grinding I. Diopside. *International Journal of Mineral Processing* 61, 273–288.
- [15] Kalinkina, E.V., Kalinkin, A.M., Forsling, W., and Makarov, V.N. (2001) Sorption of atmospheric carbon dioxide and structural changes of Ca and Mg silicate minerals during grinding II. Enstatite, akermanite and wollastonite. *International Journal of Mineral Processing* 61, 289–299.
- [16] Kalinkin, A.M., Kalinkina, E.V., and Makarova, T.I. (2006) Structural Transformations of Silicates upon Prolonged Grinding. *Russian Journal of General Chemistry* 76, 523–528.
- [17] Krogh-Moe, J. (1956) A Method for Converting Experimental X-ray Intensities to an Absolute Scale. *Acta Crystallographica* 9, 951.
- [18] Marumo, F. and Okuno, M. (1984) X-ray structural studies of molten silicates: Anorthite and albite melts, In: I. Sunagawa (ed). *Material Sciences of the Earth's Interior*, TERRAPUB, 25–38.
- [19] Yin, C. D., Okuno, M., Morikawa, H., and Marumo, F. (1983) Structural Analysis of MgSiO_3 Glass. *Journal of Non-Crystalline Solids* 55, 131–141.
- [20] Yin, C. D., Okuno, M., Morikawa, H., Marumo, F., and Yamanaka, T. (1986) Structural Analysis of CaSiO_3 Glass by X-ray Diffraction and Raman Spectroscopy. *Journal of Non-Crystalline Solids* 80, 167–174.
- [21] Shimoda, K., Miyamoto, H., Kikuchi, M., Kusaba, K., and Okuno, M. (2005) Structural evolutions of CaSiO_3 and $\text{CaMgSi}_2\text{O}_6$ metasilicate glasses by static compression. *Chemical Geology* 222, 83–93.
- [22] Whittaker, E. J. W. and Muntus, R. (1970) Ionic radii for use in geochemistry. *Geochimica et Cosmochimica Acta* 34, 945–956.

- [23] Fine, G. and Stolper, E. (1985) The speciation of carbon dioxide in sodium aluminosilicate glasses. *Contributions to Mineralogy and Petrology* 91, 105–121.
- [24] Fine, G. and Stolper, E. (1985) Dissolved carbon dioxide in basaltic glasses: concentrations and speciation. *Earth and Planetary Science Letters* 76, 263–278.
- [25] Schott, J., Berner R.A, and Sjoberg, E.L. (1981) Mechanism of pyroxene and amphibole weathering—I. Experimental studies of iron-free minerals. *Geochimica et Cosmochimica Acta* 45, 2123–2135.
- [26] Taniguchi, T., Okuno, M., and Matsumoto, T. (1997) X-ray diffraction and EXAFS studies of silicate glasses containing Mg, Ca and Ba atoms. *Journal of Non-Crystalline Solids* 211, 56–63.
- [27] Velde, B. and Couty, R. (1987) High pressure infrared spectra of some silicate glasses. *Chemical Geology* 62, 35–41.
- [28] Kubicki, J.D., Hemley, R.J., and Hofmeister, A.M. (1992) Raman and infrared study of pressure-induced structural changes in MgSiO_3 , $\text{CaMgSi}_2\text{O}_6$, and CaSiO_3 glasses. *American Mineralogist* 77, 258–269.
- [29] Park, J.H., Min, D.J., and Song, H.S. (2002) FT-IR Spectroscopic Study on Structure of CaO-SiO_2 and $\text{CaO-SiO}_2\text{-CaF}_2$ Slags. *ISIJ International* 42, 344–351.
- [30] Virgo, D., Mysen, B.O., and Kushiro, I. (1980) Anionic constitution of 1-atmosphere silicate melts: implications for the structure of igneous melts. *Science* 208, 1371–1373.